Imaging of VTI media by elastic frequency-domain full-waveform inversion of global offset data

Y. Gholami[1], *R. Brossier*[2], *A. Ribodetti*[1], *Stéphane Operto*[1] *and Jean Virieux*[2]
[1]*Géoazur - CNRS - Univ Nice Sophia-Antipolis,* [2] *LGIT - Univ Joseph Fourier*

SUMMARY

It is well acknowledged that accounting for anisotropy in seismic imaging improves focusing and depth positioning of reflectors. Indeed, at present day, seismic imaging of anisotropic media still remains one of the most challenging problem in exploration geophysics because of the possible coupling between the different anisotropic parameters. In this study, we develop a frequency-domain full-waveform inversion (FWI) method for imaging 2D visco-elastic VTI media from wide-aperture data. Frequency-domain seismic modeling is performed in VTI media with a *hp*-adaptive finite-element discontinuous Galerkin (DG) method implemented on unstructured triangular meshes that allows for accurate seismic modeling in complex media with reflectors of arbitrary shape. The inversion relies on a quasi-Newton algorithm which allows for proper scaling of misfit-function gradients associated with different parameter classes. The model parameters are either the P and S wave speeds on the symmetry axis and the Thomsen's parameters δ and ε, or the stiffness coefficients c_{11}, c_{33}, c_{13} and c_{44}.

INTRODUCTION

Full Waveform Inversion (FWI) is a re-emerging method which seeks to minimize the misfit between the recorded and the modeled data to develop high-resolution quantitative models of the subsurface (Virieux and Operto (2009) for a review). Most of the recent FWI applications have been performed in the framework of the acoustic (isotropic) approximation where only the P-wave velocity is reconstructed. Only few attempts have been made to reconstruct anisotropic parameters by FWI from cross-hole and surface acquisitions (Ji and Singh, 2005; Barnes et al., 2008; Pratt et al., 2008; Min et al., 2009). An illustration of the footprint of anisotropy on FWI is illustrated by synthetic example where the synthetic Valhall model is reconstructed by acoustic isotropic FWI from anisotropic data.

In this study, we develop a 2D frequency-domain FWI method for imaging visco-elastic transversely isotropic media with vertical symmetry axis (VTI). The forward modeling is based on a low-order finite-element DG method on unstructured triangular meshes, that allows for accurate modeling of complex wave phenomena in both onshore and offshore media (Brossier et al., 2008). The VTI medium is either parameterized by four stiffness coefficients or by the P and S wave speeds on the symmetry axis, V_{P_0} and V_{S_0}, and the Thomsen's parameters δ and ε (Thomsen, 1986). Density and attenuation factors Q_P and Q_S are the other parameters which can be taken into account in the modeling and inversion. We first review the basics of frequency-domain FWI and the radiation pattern of each class of anisotropic parameters in the framework of the ray+Born approximation. Second, we present some preliminary FWI results that are interpreted in the light of the radiation-pattern analysis. Thirdly, we present some examples of FWI with simple synthetic model. Results highlight the coupling between the parameters and the difficulty of imaging the δ parameter from surface data.

Finally we illustrate the footprint of anisotropy on FWI by reconstructing the synthetic Valhall model with acoustic isotropic FWI from anisotropic data

METHOD

Forward modeling of 2D VTI media is developed by frequency-domain DG method, considering the frequency-domain first order velocity-stress system in anisotropic media:

$$\begin{aligned}
-i\omega V_x &= \frac{1}{\rho(\mathbf{x})}\left\{\frac{\partial \sigma_{xx}}{\partial x}+\frac{\partial \sigma_{xz}}{\partial z}\right\}+f_x \\
-i\omega V_z &= \frac{1}{\rho(\mathbf{x})}\left\{\frac{\partial \sigma_{xz}}{\partial x}+\frac{\partial \sigma_{zz}}{\partial z}\right\}+f_z \\
-i\omega \sigma_{xx} &= c_{11}\frac{\partial V_x}{\partial x}+c_{13}\frac{\partial V_z}{\partial z}-i\omega\sigma_{xx_0} \\
-i\omega \sigma_{zz} &= c_{13}\frac{\partial V_x}{\partial x}+c_{33}\frac{\partial V_z}{\partial z}-i\omega\sigma_{zz_0} \\
-i\omega \sigma_{xz} &= c_{44}\left\{\frac{\partial V_x}{\partial z}+\frac{\partial V_z}{\partial x}\right\}-i\omega\sigma_{xz_0}, \qquad (1)
\end{aligned}$$

where particle velocities (V_x,V_z) and stresses (σ_{xx},σ_{zz},σ_{xz}) are unknown quantities. The c_{11},c_{13}, c_{33} and c_{44}, are stiffness coefficients for 2D VTI media, ρ is the density, ω is the angular frequency, and $i=\sqrt{-1}$ is the purely imaginary term. Source terms are either point forces (f_x, f_z) or applied stresses $(\sigma_{xx_0}, \sigma_{zz_0}, \sigma_{xz_0})$. Absorbing boundary conditions are implemented along the bottom, right and left edges of the computational domain with Perfectly-Matched Layers (Berenger, 1994) while a free surface boundary condition or an absorbing PML can be implemented on top of the model.
The medium is discretised on unstructured triangular mesh. For each cell, the system of equations is multiplied by a test function, corresponding to a k^{th}-order Lagrange polynomial. The test function is nonzero only in the polygonal cell that ensures the discontinuous property of the scheme. The system of equations is then integrated over each cell, which leads to the so-called weak formulation of the system. Discretization of the system with the DG method leads to a sparse linear system $\mathbf{Au}=\mathbf{b}$ for each modeled frequency, where $\mathbf{A}$ is the so-called impedance matrix, $\mathbf{u}$ is the velocity-stress wavefield vector and $\mathbf{b}$ is the source vector. The system is solved with the massively parallel direct solver MUMPS (Amestoy et al., 2006) for efficient multi-source modelling required by FWI applications. Frequency-domain seismic modeling is performed in VTI media with a *hp*-adaptive finite-element DG method implemented

on unstructured triangular meshes (Brossier et al., 2008). The VTI medium is parameterized by the P- and S-wave velocities on the symmetry axis, the density, the attenuation factors Q_P and Q_S and the Thomsen's parameters δ and ε (Thomsen, 1986). The wavefield that can be inverted are the horizontal and vertical particle velocities and the pressure. The minimization of the L_2 misfit function is performed with a L-BFGS quasi-Newton algorithm which provides an approximation of the product between the inverse of the Hessian $\mathbf{H}$ and the gradient $\mathbf{G}$ of the misfit function (Nocedal and Wright, 1999). The gradient $\mathbf{G}^{(n)}$ is efficiently computed with the adjoint-state method (Plessix, 2006):

$$\mathbf{G}_{m_i} = \sum_{if=1}^{nf} \sum_{is=1}^{ns} \Re\{\mathbf{u}^t r\} \tag{2}$$

The gradient is formed by the product of the incident wavefield $\mathbf{u}$ with the back-propagated adjoint wavefield r, defined as r=$\frac{\partial \mathbf{A}^t}{\partial m_i}\mathbf{A}^{-1}\Lambda_{data}\mathbf{W}_d\Delta\mathbf{d}^*$. $\mathbf{A}$ is the impedance matrix (the forward problem operator), ^{t} and * denote the transpose and conjugate operators, respectively, $\Re$ denotes the real part of a complex number, and Λ_{data} is an operator that projects the residual vector to the forward problem space (Pratt et al., 1998). The radiation pattern of the scatterer associated with the parameter m_i describes the sensitivity of the data to the model parameter m_i as a function of the aperture (or diffraction) angle. Radiation pattern can be derived analytically in the framework of high-frequency ray theory (see following section) or numerically by computing the secondary virtual source $\frac{\partial \mathbf{A}^t}{\partial m_i}\mathbf{u}$ of the partial derivative wavefield . The radiation patterns for each parameter class are helpful to define the parameter classes that can be reliably reconstructed by FWI.

RADIATION PATTERNS OF VTI PARAMETERS

The analytical expression of the radiation pattern of the VTI parameters has been derived in the framework of the asymptotic ray+Born approximation by Calvet et al. (2006). The P-P scattering coefficients for parameters α, δ and ε are given by

$$\begin{aligned} W_\alpha^{P\to P} &= 1 \\ W_\delta^{P\to P} &= \tfrac{1}{2}[\sin 2(\xi+\Delta\xi)\cos 2(\Psi+\Delta\Psi) \\ &\quad + \sin 2(\Psi+\Delta\psi)\cos 2(\xi+\Delta\xi)] \\ W_\varepsilon^{P\to P} &= \cos 2(\Psi+\Delta\psi)\cos 2(\xi+\Delta\xi) \\ &\quad - \cos 2(\Psi+\Delta\psi) - \cos 2(\xi+\Delta\xi) \end{aligned} \tag{3}$$

where Ψ is the angle between the incident polarization vector and the symmetry axis and ξ is the angle between the scattering polarization vector and the symmetry axis (Figure 1). $\Delta\psi$ and $\Delta\xi$ are the deviation angles made by the wave polarization vector and the wave vector. The P-P scattering coefficients in equation 3 represents the radiation pattern of the virtual source $\frac{\partial \mathbf{A}^t}{\partial m_i}\mathbf{u}$, equation 2, in the framework of frequency-domain FWI (Pratt et al., 1998).

Radiation patterns of each parameter classes are shown in Figures 2(a-g) for different incidence angles Ψ. At the stationary

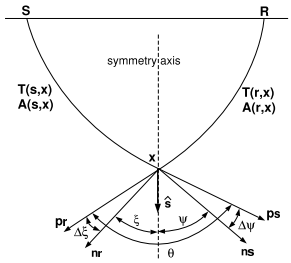

Figure 1: Diffraction in VTI media. $\mathbf{p_s}$, $\mathbf{p_r}$: incident and scattered polarization vectors; $\mathbf{n_s}$, $\mathbf{n_r}$: incident and scattered wave vectors. $\mathbf{S}$ and $\mathbf{R}$: source and receiver positions; $\mathbf{x}$: diffractor. θ: diffraction angle. ψ and ξ: angles between the incident and scattered wave vectors with the symmetry axis. $\hat{\mathbf{s}}$: unit vector along the symmetry axis.

points on the reference ray path ($\Psi = \xi$), the P-P scattering coefficients reduce to (Figure 2h)

$$W_{V_{P_0}}^{P\to P} = 1;\ W_\delta^{P\to P} = \left(\frac{1}{2}sin(\theta)\right)^2;\ W_\varepsilon^{P\to P} = sin^4(\theta/2) - 1. \tag{4}$$

The radiation patterns shown in Figure 2h are representative of a specular reflection in a VTI medium from a surface acquisition.

The radiation pattern of V_{P_0} is isotropic, whatever the incident angle Ψ is, and is the same as that of V_P in acoustic isotropic media. For small values of Ψ, the radiation pattern of ε is closes to that of V_{P_0}, whatever the diffraction angle θ is. Therefore, a strong coupling between these two parameters is expected when the incident wavefield propagates in the direction close to the symmetry axis. As Ψ increases to 90^o, the amplitude of the radiation pattern of ε decreases and vanishes for diffraction angle of 90^o and 270^o. This suggests that for wide-aperture surface acquisitions, parameters V_{P_0} and ε should be reasonably well uncoupled at intermediate diffraction angles (i.e., between 45 and 135^o) (Figure 2h). The parameter δ does not scatter energy at short and wide aperture when the incident wavefield propagates near the direction of the symmetry axis. The highest sensitivity of the data to δ is reached at intermediate diffraction angles (i.e., between 45 and 135^o). The opposite behavior is observed for incident waves propagating perpendicularly to the symmetry axis: the highest amplitude of the radiation pattern is obtained at small diffraction angles (i.e., 0-45^o). The specular radiation pattern shows that δ scatters energy mainly at intermediate scattering angles (45^o and 135^o). At these angles, it seems difficult to uncouple the contributions of ε and δ.

CANONICAL NUMERICAL EXAMPLE

We consider a circular anisotropic inclusion embedded in a homogeneous anisotropic background. The properties of the inclusion and the background medium are mentioned in Table(1),

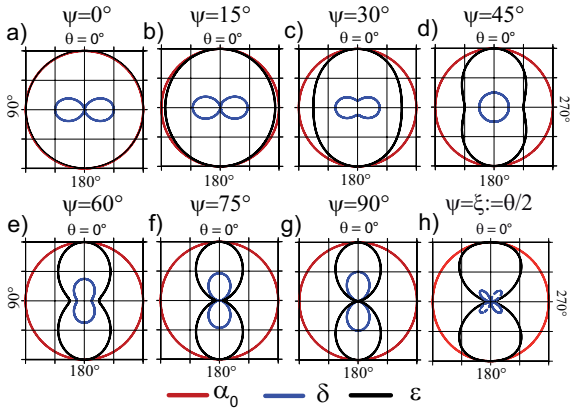

Figure 2: (a-g) P-P radiation pattern for V_{P_0}, δ and ε and for incidence angles Ψ ranging between 0^o and 90^o. h) P-P radiation pattern for V_{P_0}, δ and ε for specular angle.

density assumed to be constant as 1000 kg/m^3 . Sixty explosive sources and sixty two-components receivers are uniformly distributed on a circular acquisition geometry, the center of which matches the center of inclusion, leading to a full acquisition coverage in terms of incidence and aperture angles. Two frequency components equal to 4 and 6 Hz are inverted. The P- and S- propagated wavelengths at 6 Hz are 250 m and 166 m, respectively. The radius of the inclusion is 50 m. The reconstructed parameters in FWI are V_{P_0}, V_{S_0}, δ and ε. The four parameter classes are reconstructed simultaneously (Figures 3a-d). V_{P_0}, V_{S_0} and ε are successfully reconstructed whereas δ show unstable reconstruction although the ideal acquisition. One can note the coupling between δ (related to c_{13} stiffness coefficient) and V_{P_0}, V_{S_0} (related to c_{33} and c_{44}) in Thomsen's anisotropy parameters, to explain low amplitude of inverted δ parameter.

	$V_{p_0}(m/s)$	$V_{s_0}(m/s)$	δ	ε
B/I	1000/1200	1500/1800	0.10/0.15	0.10/0.15

Table 1: Properties of the inclusion VTI medium reconstructed by FWI, B= background and I=inclusion properties, respectively.

ANISOTROPIC SYNTHETIC VALHALL MODEL

In this study we consider the V_p synthetic Valhall model provided by BP, (Figure 4(a)). Presence of gas cloud on the top of large sediments layer and the trapped oil underneath the Chalk cap rock, is a good target for our inversion test. Low P-wave velocity is the main property of gas cloud. We provided anisotropic synthetic Valhall model benchmark by constructing the δ and ε models for proper layers, (Figures 4(b) and (c)). We generated acoustic anisotropic numerical data by using DG method presented above. We firstly did acoustic anisotropic inversion of anisotropic data and we recover only V_p model parameter. Figure (5) shows the smoothed V_p,δ and ε models, used as starting models for FWI. Smoothing was obtained with a 2D Gaussian filter of horizontal correlation lengths 500m and of vertical correlation, linearly increasing with depth, starting from 25m at the water/solid interface, to 1000m at 5200m-depth. Density is assumed to be constant during inversion. The OBC acquisition geometry composed of 315 pressure sources, located 6m below the water depth, spacing 50m horizontally. 315 hydrophone are located at depth of 70m on the sea bottom for acoustic inversion. Five frequencies are involved in the inversion, starting at 2 Hz up to 6 Hz. In figure 6(a), the result of acoustic anisotropic V_p parameter is shown, and the vertical profiles of true, starting and inverted model at 8.125 and 9 km offsets are shown in figures 6(c) and (d). For this test the anisotropic parameters δ and ε are fixed to smoothed model. Then we did a second test and we made an isotropic inversion of anisotropic observed data (Figures 6(b)). As it can be seen, the anisotropic inversion of anisotropic observed data helps to well reconstruct V_p parameter. This can be seen in more details by plotting vertical velocity profiles (Figures 6 (b)-(d)). Below 2km-depth, until the top of cap rock, Thomsen's parameters, δ=0.05 and ε=0.25, present high values. Only the anisotropic inversion of anisotropic data (Figures 6(c) and (d)), can well reconstruct the velocity model in this zone. Indeed, isotropic inversion of anisotropic data (Figures 6(e) and (f)), provides less well resolved results than anisotropic inversion. The region between the cap rock and the reservoir presents weak anisotropy, δ=-0.05 and ε=0.0. Velocity model recovered by isotropic inversion is not well constructed. This is probably due to the effects of upper anisotropic layers. Anisotropic inversion provides better results also in this part of model where anisotropy is weak. Inversion of Thomsen's anisotropic parameters will be performed in the next step of this study and is proposed as future work.

DISCUSSION AND CONCLUSION

We have implemented a 2D frequency-domain FWI method for imaging VTI media. The forward modeling is based on a discontinuous Galerkin method on unstructured triangular meshes. We have reviewed the radiation pattern of the anisotropic parameters for the P-P scattering models which show the coupling between the parameters as a function of the incidence angle and the diffraction angle. Preliminary applications of FWI for an ideal circular acquisition have highlighted parameter coupling during the reconstruction. Further studies are required to define the optimal choice of parameters for FWI in anisotropic media and the best hierarchic strategy to manage

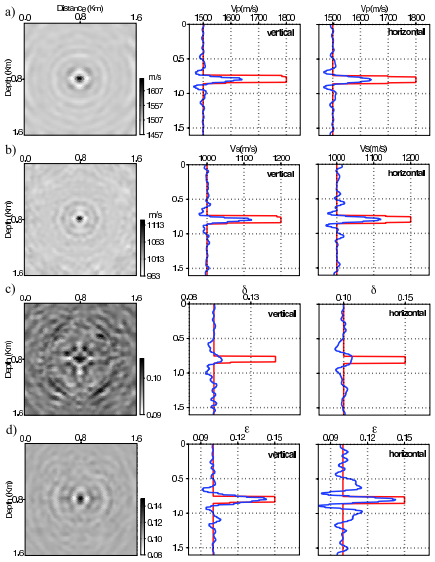

Figure 3: Imaging of an anisotropic inclusion from a circular acquisition geometry by FWI. (a-d) All the parameters V_{P_0}(a), V_{S_0}(b), δ(c) and ε(d) are reconstructed simultaneously. Center and right panels show vertical and horizontal logs for true (red) and recovered (blue) models.

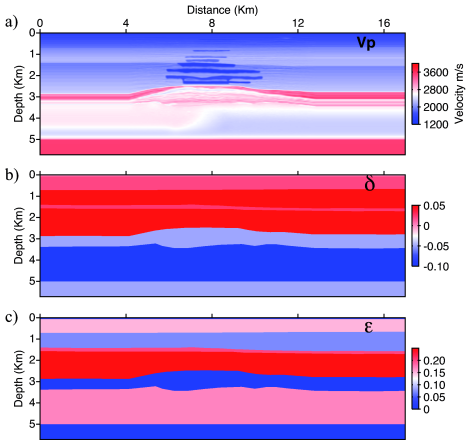

Figure 4: Synthetic Valhall true model, a) V_p, b) δ, and c) ε.

the different parameter classes during FWI.

ACKNOWLEDGMENTS

This study has been funded by the SEISCOPE consortium http://seiscope.oca.eu, sponsored by BP, CGG-VERITAS, EXXON-MOBIL, SHELL and TOTAL, and by ANR under project ANR-05-NT05-2-42427. Access to the high-performance computing facilities of MESOCENTRE SIGAMM (OCA) and IDRIS (CNRS) computer centers provided the required computer resources.

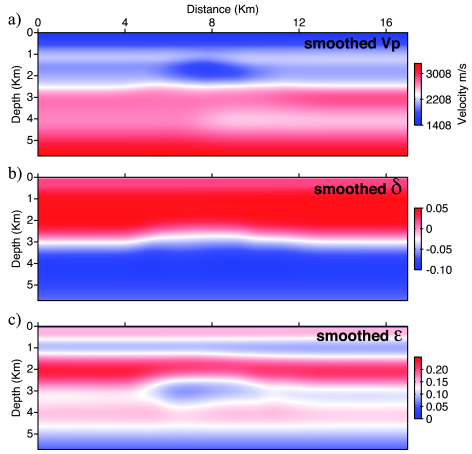

Figure 5: Smoothed synthetic Valhall models as initial model for FWI, a) V_p, b) δ, and c) ε.

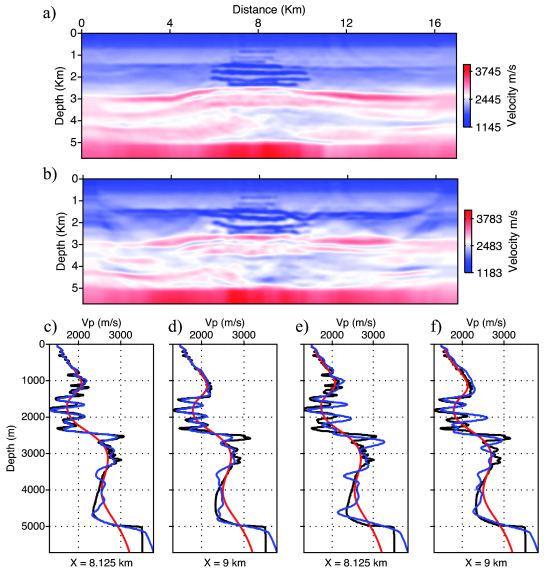

Figure 6: Imaging of synthetic P-velocity Valhall model, a) acoustic anisotropic inversion of only V_p using smoothed δ and ε, with its vertical profiles at 8.125 and 9km offset,c) and d). b) acoustic isotropic inversion of anisotropic data,and vertical profiles at 8.125 and 9km offset, e) and f).

EDITED REFERENCES

Note: This reference list is a copy-edited version of the reference list submitted by the author. Reference lists for the 2010 SEG Technical Program Expanded Abstracts have been copy edited so that references provided with the online metadata for each paper will achieve a high degree of linking to cited sources that appear on the Web.

REFERENCES

Amestoy, P. R., A. Guermouche, J. Y. L'Excellent, and S. Pralet, 2006, Hybrid scheduling for the parallel solution of linear systems: Parallel Computing, **32**, no. 2, 136–156, doi:10.1016/j.parco.2005.07.004.

Barnes, C., M. Charara, and T. Tsuchiya, 2008, Feasibility study for an anisotropic full waveform inversion of cross-well seismic data: Geophysical Prospecting, **56**, no. 6, 897–906, doi:10.1111/j.1365-2478.2008.00702.x.

Berenger, J.-P., 1994, A perfectly matched layer for absorption of electromagnetic waves: Journal of Computational Physics, **114**, no. 2, 185–200, doi:10.1006/jcph.1994.1159.

Brossier, R., J. Virieux, and S. Operto, 2008, Parsimonious finite-volume frequency-domain method for 2-D P-SV-wave modelling: Geophysical Journal International, **175**, no. 2, 541–559, doi:10.1111/j.1365-246X.2008.03839.x.

Calvet, M., S. Chevrot, and A. Souriau, 2006, P-wave propagation in transversely isotropic media i. finite-frequency theory: Physics of the Earth and Planetary Interiors, **156**, no. 1-2, 12–20, doi:10.1016/j.pepi.2006.01.004.

Ji, Y., and S. C. Singh, 2005, Anisotropy from full waveform inversion of multicomponent seismic data using a hybrid optimization method: Geophysical Prospecting, **53**, no. 3, 435–445, doi:10.1111/j.1365-2478.2005.00476.x.

Min, H. Y. L. D. J., M. Koo, N. E. Kwak, and B. D. Kwon, 2009, Time-domain elastic full-waveform inversion for transversely isotropic media : EAGE Expanded Abstracts.

Nocedal, J., and S. J. Wright, 1999, Numerical optimization: Springer.

Plessix, R.-E., 2006, A review of the adjoint-state method for computing the gradient of a functional with geophysical applications: Geophysical Journal International, **167**, no. 2, 495–503, doi:10.1111/j.1365-246X.2006.02978.x.

Pratt, R. G., C. Shin, and G. J. Hicks, 1998, Gauss-Newton and full Newton methods in frequency-space seismic waveform inversion: Geophysical Journal International, **133**, no. 2, 341–362, doi:10.1046/j.1365-246X.1998.00498.x.

Pratt, R. G., L. Sirgue, B. Hornby, and J. Wolfe, 2008, Cross-well waveform tomography in fine-layered sediments - meeting the challenges of anisotropy: 70th Annual International Meeting, EAGE, F020.

Thomsen, L. A., 1986, Weak elastic anisotropy: Geophysics, **51**, 1954–1966, doi:10.1190/1.1442051.

Virieux, J., and S. Operto, 2009, An overview of full waveform inversion in exploration geophysics: Geophysics, **74**, no. 6, WCC1, doi:10.1190/1.3238367.